ATMOSPHERIC SCIENCE

On the crucial role of atmospheric rivers in the two major Weddell Polynya events in 1973 and 2017 in Antarctica

Diana Francis[1]*, Kyle S. Mattingly[2], Marouane Temimi[3], Rob Massom[4], Petra Heil[4]

This study reports the occurrence of intense atmospheric rivers (ARs) during the two large Weddell Polynya events in November 1973 and September 2017 and investigates their role in the opening events via their enhancement of sea ice melt. Few days before the polynya openings, persistent ARs maintained a sustained positive total energy flux at the surface, resulting in sea ice thinning and a decline in sea ice concentration in the Maud Rise region. The ARs were associated with anomalously high amounts of total precipitable water and cloud liquid water content exceeding 3 SDs above the climatological mean. The above-normal integrated water vapor transport (IVT above the 99th climatological percentile), as well as opaque cloud bands, warmed the surface (+10°C in skin and air temperature) via substantial increases (+250 W m^{-2}) in downward longwave radiation and advection of warm air masses, resulting in sea ice melt and inhibited nighttime refreezing.

INTRODUCTION

Atmospheric rivers (ARs) are narrow corridors of strong horizontal water vapor transport associated with a low-level jet stream ahead of the cold front of an extratropical cyclone and located within the cyclone's warm conveyer belt (1). In both hemispheres, ARs are believed to account for more than 90% of the annual moisture transport from the tropics into high latitudes, during a relatively small number of transient events that cover up to only 10% of the globe's surface (2).

In polar regions, where AR activity has been increasing in recent years (3, 4), the ability of ARs to rapidly transport large amounts of moisture and heat poleward has significant consequences for both land and sea ice. Their role in short-duration but high-volume melt events over the Arctic and Antarctic has been highlighted in recent years (5). Research to date has shown that ARs can increase ice melt by several physical mechanisms, including (i) enhancement of the water-vapor greenhouse effect, (ii) the formation of extensive cloud bands that retain outgoing longwave (LW) radiation and re-emit it back to the surface, (iii) the release of condensational latent heat in the advected air mass (6), (iv) increase in surface melt energy via liquid precipitation (7), and (v) the generation of turbulent heat fluxes into the ice (8). Moreover, ARs can indirectly foster ice melt by enhancing the deepening of the cyclone ahead of which they develop, with intense ARs strengthening the cyclone by providing more water vapor for latent heat release (9). In addition, ARs are closely related to the atmospheric fronts over the Southern Ocean (10), which, in turn, reinforces subantarctic cyclone dynamics. The highest frequency of these fronts is typically found in the latitude belt 40°S to 60°S in both summer and winter, and they can extend poleward to lengths exceeding 2000 km (10).

Cyclones around Antarctica are known to significantly alter the sea ice field both dynamically (e.g., through wave action and ice drift) and thermodynamically (11, 12). This is particularly important in winter, when cyclones are thought to be the primary transporter of heat and moisture into the polar regions (13, 14) and therefore contribute to sea ice melt in the absence of solar radiation (15, 16).

Despite their rarity (i.e., around 12 major events per year in West Antarctica), ARs are a key factor in driving both surface melting on the major ice shelves of West Antarctica (4) and mass loss on the Greenland Ice Sheet because of enhanced downward LW radiation and turbulent heat fluxes (17–19). On the other hand, ARs can also contribute to local snow accumulation on the ice sheet (20)—although sharp losses in surface mass balance caused by AR radiative forcing can locally exceed the moderate gain from snow accumulation during summer (3, 4).

Regarding sea ice, a growing body of recent Arctic work (21, 22) shows that atmospheric moisture intrusions, along with associated cloud liquid water and ice content, can sharply increase downwelling LW radiation—to initiate surface melt and inhibit subsequent refreezing (23–25). This work further shows that warm moist air intrusions associated with blocking events can induce significant decline in Arctic sea ice (26) as the efficiency of the atmosphere to radiatively cool to space decreases, thereby increasing the amount of energy retained in the atmosphere and reradiated back toward the surface (25).

Furthermore, in situ measurements of winter sea ice in the Arctic have shown that, when ARs occur over the ice, they generate distinct thermal waves that propagate into the ice and decrease the ice basal growth rate. Pulses of warming induced by warm moist air intrusions have been observed down to a depth of 150 cm in Arctic sea ice, with a 5-day time lag (8). This process could have an even more significant impact on Antarctic sea ice, which is known to be thinner than Arctic sea ice with an estimated mean thickness of less than 2 m (27). Despite the crucial role of ARs in altering ice conditions and the atmosphere-ice-ocean energy balance, no attention has been given to their impact on sea ice in Antarctica particularly during the winter season when the albedo effect is negligible and the LW radiation effect dominates.

[1]Khalifa University of Science and Technology, P. O. Box 54224, Abu Dhabi, United Arab Emirates. [2]Institute of Earth, Ocean, and Atmospheric Sciences, Rutgers University, New Brunswick, NJ 08901-8554, USA. [3]Department of Civil, Environmental, and Ocean Engineering (CEOE), Stevens Institute of Technology, Hoboken, NJ 07030, USA. [4]Australian Antarctic Division and Australian Antarctic Program Partnership, Private Bag 80, c/o University of Tasmania, Hobart, Tasmania 7001, Australia.
*Corresponding author. Email: diana.francis@ku.ac.ae

Within the sea ice zones of both hemispheres, persistent and recurrent regions of open water are knowns as polynyas. They are tens of thousands of square kilometers in areal extent and usually occur at specific locations preconditioned by the ocean circulation (28). For marine ecosystems, they constitute recurrent "windows" in the sea ice cover and entail ecologically important "oases" that enable marine life to overwinter at high latitudes and encourage enhanced primary production in the spring (29).

In the Southern Ocean, most of the polynyas occur near the coast except a few, such as the Weddell Polynya, which occurs within the midocean sea ice cover of the eastern Weddell Sea (28). The latter overlies the Maud Rise seamount (centered on 66°S and 3°E and reaching to within 1200 m of the surface), which together with the Weddell Gyre entrain relatively warm Weddell Deep Water to the surface via deep convection (30). This provides an ideal location for the initialization of a midocean polynya (31, 32) where the sea ice is generally thin and has low concentration even during the winter months (33).

The Weddell Polynya was observed for the first time in 1974 in Nimbus 5 satellite sea ice concentration imagery, and the second major opening occurred in September 2017 (32, 34). In those years, its maximum area varied between ~200,000 and 300,000 km². By virtue of its vast size and location, the polynya makes a major contribution to the wintertime transfer of heat and moisture between the ocean and atmosphere and ventilation of the deep interior ocean. In doing so, it strongly modulates regional and wider oceanic and atmospheric properties and circulation (35).

Given these factors, there is strong motivation to better understand and model the nature and drivers of Weddell Polynya openings, to improve their representation in models, determine their wide-ranging effects, and more accurately predict whether these rare but important events will occur more frequently (or not) in a warming climate. Various processes have been proposed to explain the polynya formation and maintenance, all involving the complex atmosphere–ocean sea ice–seabed interaction system. These include (i) changes in atmospheric circulation associated with La Niña and negative Southern Annular Mode (SAM) (34), (ii) upper-ocean preconditioning (36) concurrent with severe storms (37, 38), and (iii) intensification of westerly winds causing a spin-up of the Weddell Gyre (36).

Recent studies on the Weddell Polynya 2017 event have highlighted the contributions of wind forcing from cyclones (37) and the oceanic forcing from warm water upwelling (38). An additional potentially important factor that has been neglected to date is the presence and role of coincident AR events. That is the focus of this study, which (i) connects these previously identified processes to larger-scale poleward atmospheric heat and moisture transport by ARs and (ii) quantifies how ARs contribute to sea ice surface melt and inhibit sea ice formation through cloud, precipitation, and surface energy balance effects.

In this work, we show the occurrence of intense ARs (Fig. 1, A and B) during the cold late-winter months over the Weddell Sea. We then carry out a first investigation of their role in generating sea ice melt and contributing to the major opening events of the Weddell Polynya observed in the 1970s (Fig. 1C) and in September 2017 (Fig. 1D). In Results and Discussion, we present and discuss our results for the 2017 and the 1973 polynya events. Because of the lack of high-resolution data for the event in 1973, we mainly use it to corroborate our findings for the 2017 event and to highlight a few differences

between these two extraordinary events. The "Summary and conclusions" section summarizes our findings, and Materials and Methods details the data and methods used in this study.

RESULTS AND DISCUSSION
ARs during September 2017
The large-scale circulation in the Southern Hemisphere during austral winter 2017 and, more particularly, in September 2017 was marked by an amplified zonal wave three pattern [as described in detail in (37) and the "ARs and polynya occurrence in November 1973" section] during which poleward transport of warm and moist air was considerably intensified. At that time, the existing below-average deep low and above-average ridge in the South Atlantic sector (37) steered intense and narrow moisture bands from South America and the central Atlantic to the Weddell Sea over periods of several days. In addition, the SAM was positive during this episode (33, 37). A positive correlation exists between a positive SAM index and both cyclone and fronts frequency in the Weddell Sea and its upstream environs (39). Moreover, a positive interannual correlation is particularly marked between a positive SAM index and the intensity of fronts (39).

Figure 2 and fig. S1 show the four most intense AR events identified during this period to be associated with core midlatitude integrated water vapor transport (IVT) values exceeding 800 kg m⁻¹ s⁻¹ and stretching thousands of kilometers from 30°S to 70°S. The ARs covered the entire winter sea ice zone in the Weddell Sea between 5°W and 10°E. The sea ice edge in the region at this time was near 60°S (37). Besides these spectacular events—observed on 31 August and 13, 16, and 28 September 2017—several ephemeral moisture plumes associated with lesser IVT values were also identified and can be detected in the time series plot in Fig. 3. The spatiotemporal evolution of the ARs during the full period can be examined in an animation of IVT maps provided as the Supplementary Materials.

On 31 August 2017, an intense AR is seen in the IVT maps (Fig. 2A) to originate over the southeastern coast of South America and then expand over the South Atlantic. From there, a deep 500-hPa trough around 10°W and a blocking high-pressure ridge downstream around 10°E directed the influx of moisture along 0°E toward the Antarctic coast. The IVT direction within the AR was observed to drive the moisture poleward and roughly perpendicular to the Antarctic coast (Fig. 2A). The deep 500-hPa trough present around 60°S and 10°W and directly to the west of the AR (Fig. 2, A and B) developed into a very deep and large cyclone on the following day (not shown), directing even more moisture into the Maud Rise region. The AR was associated with positive normalized anomalies of precipitable water (PWAT), where PWAT exceeded 2 SDs from the mean, implying highly anomalous water vapor content relative to climatology (Fig. 2B).

On 13 September 2017, i.e., 1 day before the initial large opening of the Weddell Polynya in 2017 that was centered on 65°S to 5°E (37), a strong AR with a core IVT exceeding 800 kg m⁻¹ s⁻¹ approached the Antarctic coast in the Weddell Sea having emanated from the South Atlantic (Fig. 2C). The presence of a blocking high-pressure ridge to the east of the AR and centered on 20°W to 40°S directed anomalous poleward moisture transport (Fig. 2D). The PWAT associated with the AR on 13 September was anomalously high, with values exceeding 2.5 SDs above the climatological mean (Fig. 2D).
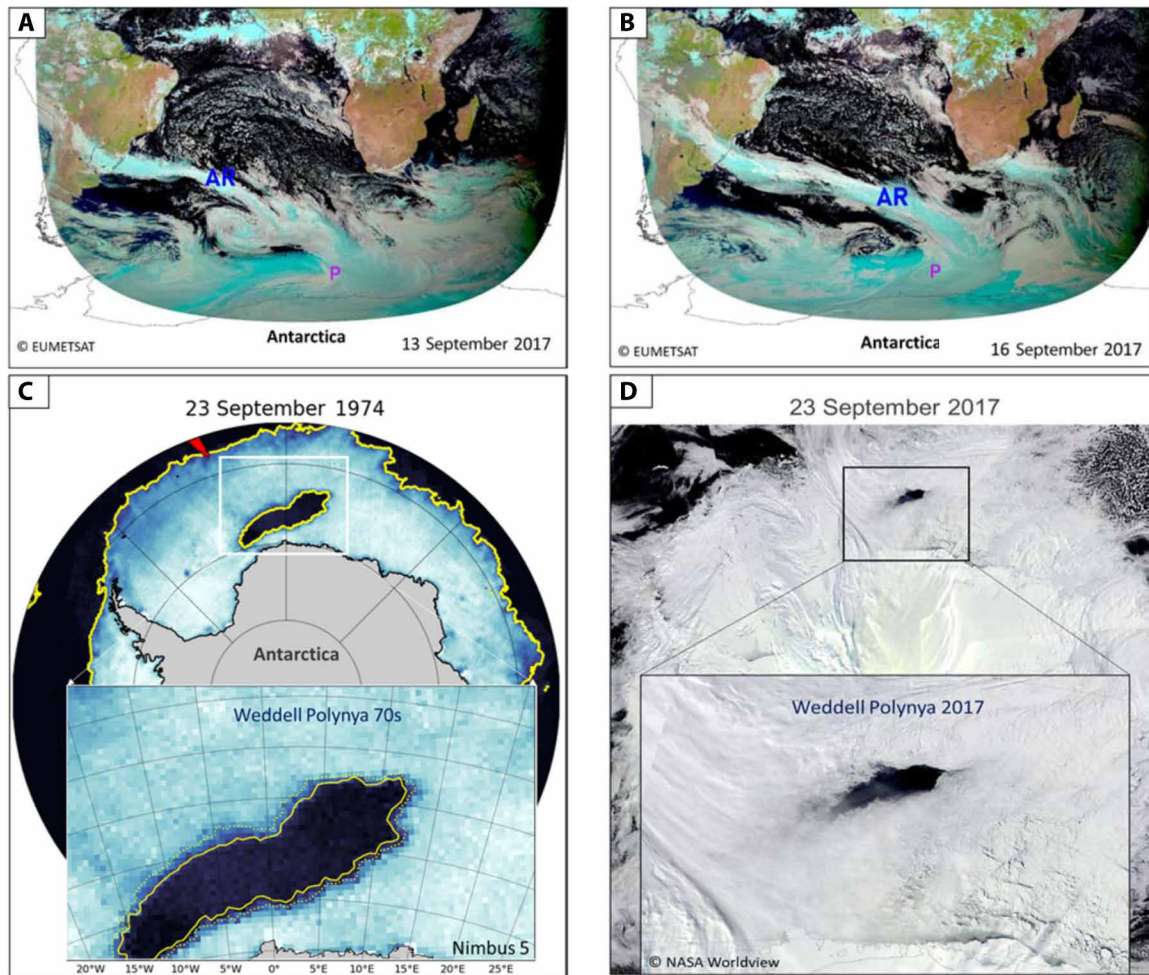
Fig. 1. ARs and the Weddell Polynya. Cloud bands associated with ARs on 13 September 2017 (**A**) and on 16 September 2017 (**B**) observed in natural colors by the Spinning Enhanced Visible and InfraRed Imager (source, The European Organisation for the Exploitation of Meteorological Satellites). (**C**) The large Weddell Polynya on 23 September 1974, which initially opened on 22 November 1973 and remained open for the following three winters, and (**D**) the second large opening, which occurred in September 2017. The location of the polynya is indicated by the letter P on (A) and (B).

Near the coast, the high PWAT band associated with the AR spread over several degrees in longitude between 20°W and 25°E (Fig. 2D). Wake turbulence in the form of counterrotating vortices trailing from the central axis of the AR can be seen in the PWAT field and wind vectors (Fig. 2D); this may have been caused by cyclonically rotating masses associated with the horizontal pressure difference and strong lower level jet within the AR.

On 16 September 2017, the day when the Weddell Polynya doubled in size (*37*), extremely high values of IVT were observed to be concentrated in a long narrow band stretching from subtropical latitudes (35°S) to the interior Antarctic Ice Sheet, with its core axis around 0°E, i.e., above the polynya (Fig. 2E). The AR signature in the PWAT appeared as a long arc-shaped strip of anomalously high water vapor content over that part of the sea ice zone where the polynya had opened on 14 September and extending toward the coast (Fig. 2F). The situation was similar for the AR on 28 September 2017 (fig. S1A), when a plume with core IVT values of 400 kg m^{-1} s^{-1} propagated poleward to cross the Antarctic coast around 0°E with IVT values of around 100 kg m^{-1} s^{-1}. This represents the extreme state of the

coastal Antarctic lower troposphere associated with ARs (*40*). At this time, the entire Eastern Weddell Sea was characterized by above-average precipitable water content (fig. S1B).

Because of the strongly decreased water vapor capacity of colder air over the sea ice zone, the magnitude of IVT associated with the AR decreased from over 800 kg m^{-1} s^{-1} equatorward of the sea ice edge to ~200 kg m^{-1} s^{-1} over the Maud Rise region. However, the associated PWAT anomalies were strongly positive in this area, demonstrating the exceptional nature of these events and their ability to rapidly inject anomalously large amounts of moisture into the otherwise relatively dry atmosphere of Antarctica during winter. The decrease in IVT values near the coast is also associated with precipitation during the AR's traverse of the sea ice zone. The AR event on 13 September 2017 was associated with a total hourly water-equivalent precipitation rate higher than 2 mm (fig. S2A), while the precipitation rate during the event on 16 September 2017 exceeded 1.5 mm/hour (fig. S2B). Most of the precipitation during the AR events was in the form of warm snow, as the 2-m air temperature over the area affected by the ARs did not fall below −5°C (fig. S2).
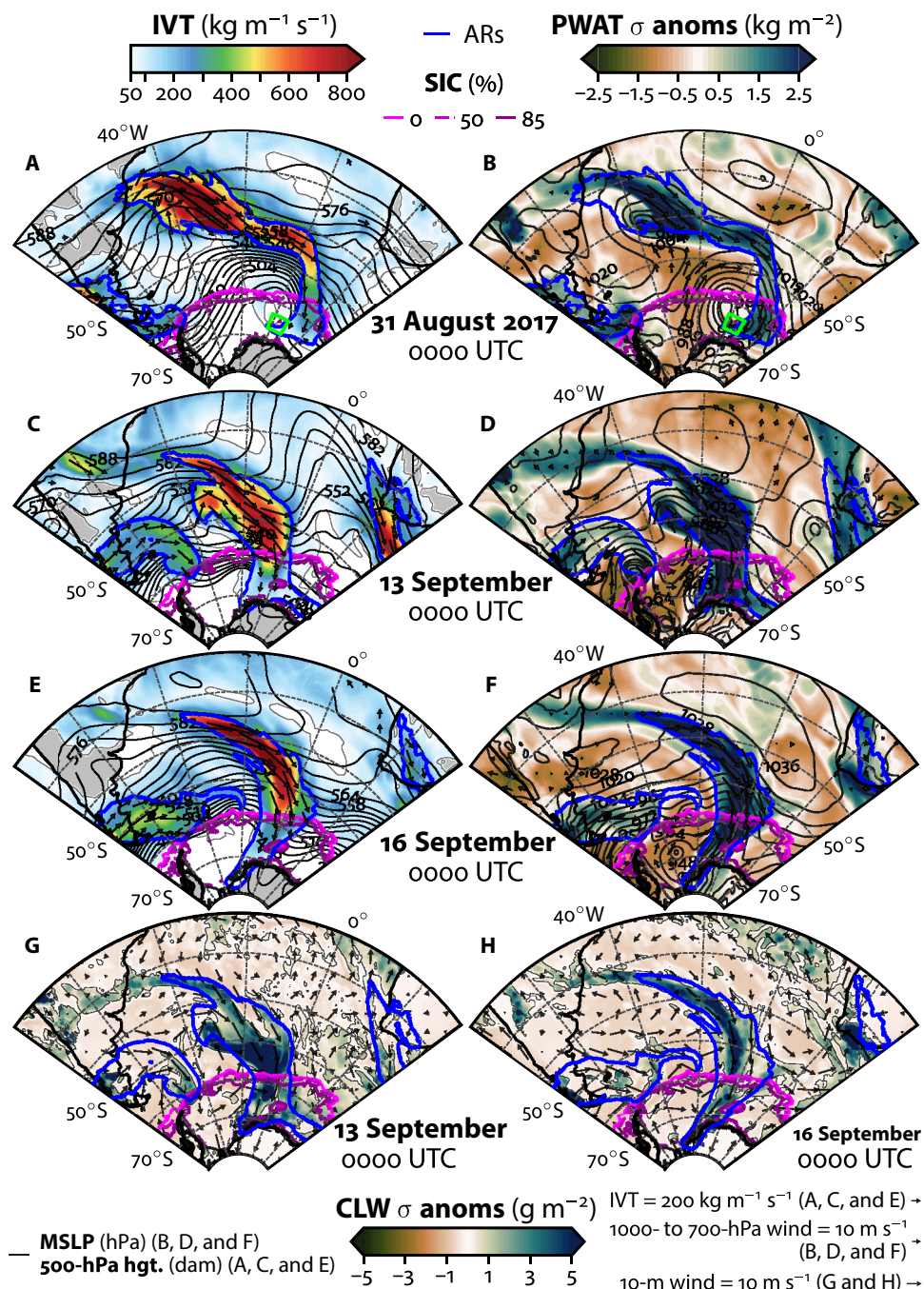
Fig. 2. The characteristics of the 2017 AR events. ERA5 reanalysis maps for 2017 of the following: (i) IVT magnitude (shaded) and direction (black vectors) and geopotential heights at 500 hPa in black contours on (**A**) 31 August at 0000 UTC, (**C**) 13 September at 0000 UTC, and (**E**) 16 September at 0000 UTC. (ii) Standardized anomalies of precipitable water (shaded), 1000- to 700-hPa mean winds in vectors and mean sea level pressure (MSLP) in black contours on (**B**) 31 August at 0000 UTC, (**D**) 13 September at 0000 UTC, and (**F**) 16 September at 0600 UTC. (iii) Standardized anomalies of total column cloud liquid water (shaded), MSLP in gray contours, and 10-m winds in black vectors on (**G**) 13 September at 0000 UTC and (**H**) 16 September at 0000 UTC. On all panels, ARs are outlined in blue contours, specific values of satellite-derived sea ice concentration (SIC) are superimposed in pink contours, and the green box corresponds to the area used to average the quantities shown in Fig. 3.

As shown in the satellite visible imagery (Fig. 1, A and B), each AR was characterized by an elongated band of stratocumulus clouds constituting both cloud liquid water and ice (*37*), a composition known to have the most substantial impact on the surface radiation budget in polar regions (*3*, *8*). The clouds within the ARs were associated with total column cloud liquid water content larger than 200 g m^{-2}, which resulted in strongly positive anomalies (more than 4 SDs above the climatological mean) over the eastern Weddell Sea (Fig. 2, G and H).
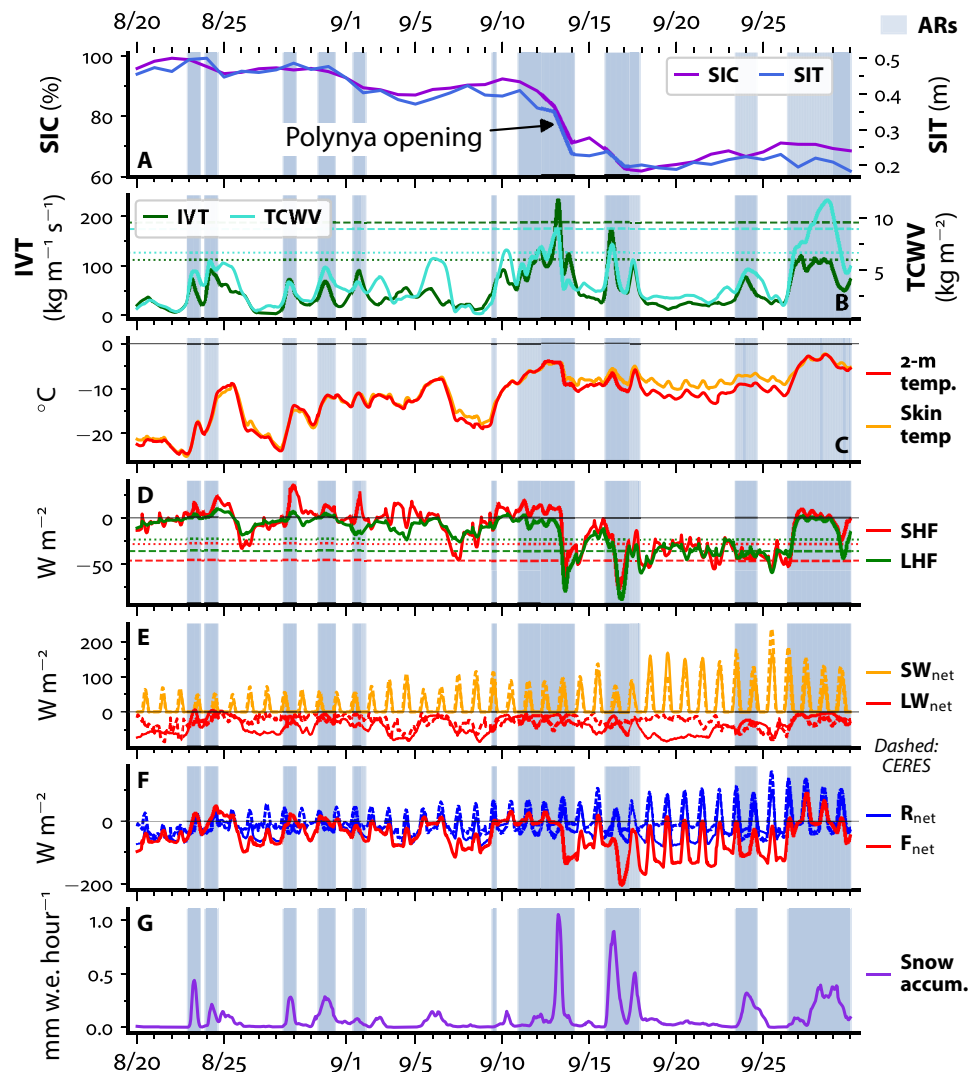
Fig. 3. The impact of the 2017 AR events. Time series from 20 August 2017 to 30 September 2017 of the following (from top to bottom): (**A**) Satellite-derived sea ice concentration and sea ice thickness (SIT). (**B**) ERA5 IVT and TCWV. (**C**) ERA5 2-m surface temperature and skin temperature. (**D**) ERA5 SHF at the surface and latent heat flux (LHF) at the surface. (**E**) Net longwave radiation (LW_{net}) and net shortwave radiation (SW_{net}) at the surface from ERA5 (solid lines) and from CERES (dashed lines). (**F**) ERA5 net radiation (R_{net}) at the surface (solid lines) and from CERES (dashed lines) and ERA5 total energy flux at the surface (F_{net}); positive values are toward the surface. (**G**) ERA5 snow accumulation rates. All quantities are averaged over the domain 2°W to 8°E, 63°S to 67°S (green box in Figs. 2 and 4). Dotted/dashed lines on panels B (D) are the 95th/99th (5th/1st) percentiles (relative to August to September climatology) showing times when IVT, TCWV, SHF, and LHF exceeded climatologically extreme values. The blue shading in the background indicates times when an AR was present over the domain. Snow accumulation is expressed in millimeter water equivalent per hour (mm w.e. hour^{-1}).

Impact of ARs on sea ice during the 2017 polynya

The Weddell Polynya in 2017 opened on 14 September 2017 (*37*). Before this date, the eastern Weddell Sea witnessed several AR events of different intensity and duration. Figure 3 shows the time series from 20 August to 30 September 2017 of different variables averaged over the area 2°W to 8°E, 63°S to 67°S, which encompasses the area of the polynya at the end of September 2017. The AR events in late August 2017 and the beginning of September 2017 were transient and associated with area-averaged IVT values below 100 kg m^{-1} s^{-1} and total column water vapor values below 7 kg m^{-2} (Fig. 3B). The area-averaged sea ice concentration decreased gradually after each of these events and reached 85% by 10 September 2017 (Fig. 3A). During the same period, the area-averaged sea ice thickness decreased by 10 cm, reaching 40 cm on 10 September 2017 (Fig. 3A).

Both skin and 2-m air temperature are seen to increase gradually at the beginning of each AR event and then decrease after the decay of the ARs (Fig. 3C).

On 11 September 2017, an intense AR event occurred over the same region and persisted during the following 2 days. The 11 to 13 September AR was in fact an extreme event with hourly area-averaged IVT values on 13 September peaking well above the 99th percentile of both the August to September 1979–2017 climatology (Fig. 3) and the July to October 1979–2017 climatology (not shown). The area-averaged skin temperature and 2-m air temperature increased by +10°C (from −15.3° to −5.3°C) during this event (Fig. 3C), and localized spikes in 2-m temperature were reported during this event with maximum surface temperature reaching −1°C (Fig. 4, E and F). During the same period, the area-averaged sensible heat flux (SHF)
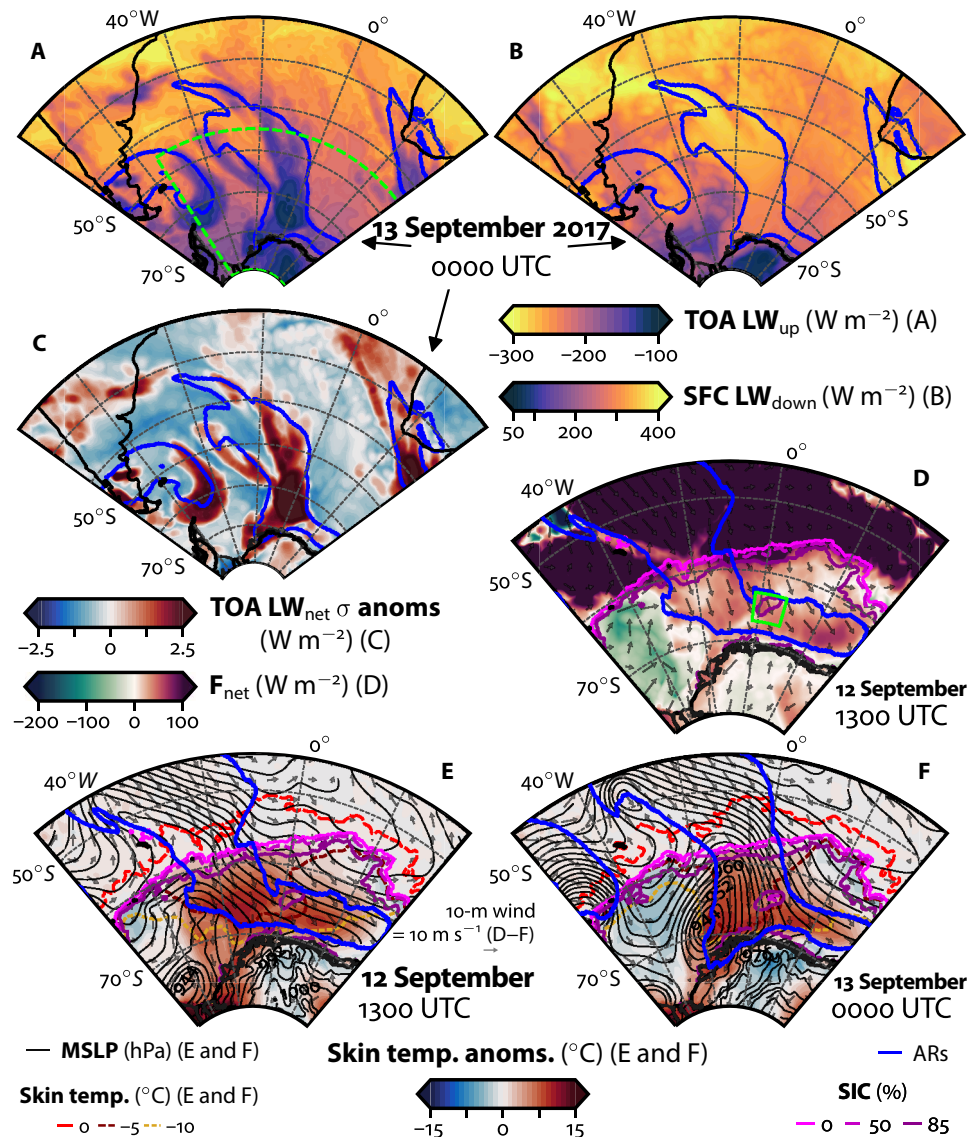
Fig. 4. The impact of the ARs on 12-13 September 2017. ERA5 reanalysis maps for the 13 September 2017 AR event of the following: (**A**) All-sky upwelling LW radiation at the TOA on 13 September at 0000 UTC. The green dashed contour represents the domain shown in (D) to (F). (**B**) All-sky downwelling LW radiation at the surface (SFC) on 13 September at 0000 UTC. (**C**) Standardized anomalies of TOA LW (shaded) on 13 September 2017 at 0000 UTC. Positive values of LW fluxes are toward Earth's surface, and negative values are away from the surface. Positive anomalies of TOA LW flux represent less outgoing LW radiation. (**D**) Total energy flux at the surface (shaded) on 12 September 2017 at 1300 UTC over the domain marked by the green dashed contour on (A). (**E**) Skin temperature anomalies on 12 September 2017 at 1300 UTC (shaded). (**F**) Same as (E) but on 13 September 2017 at 0000 UTC. On (D) to (F), MSLP is in gray contours and 10-m winds in gray vectors, and sea ice concentration, skin temperature, and 2-m temperature are superimposed for particular values as annotated on the figures. The green box represents the area used to average the quantities shown in Fig. 3. ARs are outlined in blue on all panels. All anomalies are calculated relative to the 1979–2017 climatological reference period.

at the surface switched from negative to positive (+20 W m^{-2}, Fig. 3D). The area-averaged net shortwave radiation (SW$_{net}$) at the surface decreased because of the presence of clouds (Fig. 3E), but the area-averaged net longwave radiation (LW$_{net}$) at the surface increased by more than +50 W m^{-2}, as observed in both ERA5 data and Clouds and the Earth's Radiant Energy System (CERES) satellite data (Fig. 3E). Although there were no above-freezing area-averaged temperatures during this event, there was a sustained positive (+25 W m^{-2}) heat flux at the surface (F$_{net}$) from 10 September to 13 September because of the anomalously warm and moist conditions

associated with the persistent AR (Fig. 3F). Notably, positive or near-zero melt energy values were sustained for four consecutive nights during 10 September to 13 September, indicating inhibited ability of sea ice to refreeze in the presence of enhanced atmospheric moisture and cloud cover. This input of energy is more than twice the heat input at the ice surface from the atmosphere by solar heating (less than 10 W m^{-2}) at the time of maximum annual sea ice melt in December (*41*).

The area-averaged sea ice concentration started to decline gradually at the beginning of this AR event (i.e., on 11 September 2017), reaching a first low on 13 September and dropping further on 14 September

(Fig. 3A). This extreme AR event was marked at its end by the largest daily drop in sea ice concentration on record [i.e., all sea ice seasons (July to October) since 1987], where sea ice concentration dropped by ~12% on a single day (Fig. 3A) resulting in a polynya event.

Additional AR events and associated radiative forcing occurred after the opening of the polynya (Fig. 3). For instance, an intense AR event occurred on 16 and 17 September 2017 (Fig. 2, E and F, and fig. S3) and resulted in additional 10% decrease in the area-averaged sea ice concentration (Fig. 3A) and in a doubling in the size of the Weddell Polynya (figs. S2 and S3). Toward the end of September, a persistent AR event associated with high IVT (~95th percentile) and total column water vapor greater than the 99th percentile occurred over the eastern Weddell Sea (fig. S1) and resulted in an even larger polynya (50,000 km^2), which then remained open until the end of the ice season. The occurrence of synoptic-scale intense ARs after the opening of the polynya (i.e., the sustained event on 27 to 30 September) delivered additional energy input to both the upper ocean (Fig. 3F) and the ice cover around the polynya (fig. S3). This, in turn, prevented the formation of new sea ice in the polynya area and decreased sea ice concentration around the polynya via surface, bottom, and lateral melt by both AR-induced atmospheric (as shown here) and oceanic heat (42).

The change in ocean-atmosphere interactions before and after the polynya opening was evident in the time series. Before 14 September, SHF and latent heat flux (LHF) oscillated above and below 0, but after the loss of sea ice, SHF was persistently negative until the AR event at the end of September (Fig. 3D). The F_{net} switched to a negative regime because of heat loss from the ocean after the polynya opening (Fig. 3F). According to ERA5, the amount of evaporation that occurred from the newly open ocean was unprecedented, with the daily mean LHF on 16 September 2017 being the lowest on record for any July to October day during 1979–2017 (Fig. 3D).

The AR events were accompanied by large amounts of precipitation (Fig. 3G). On the basis of ERA5 analysis, the precipitation type during these events was snow. However, it was probably very warm snow as surface temperatures were in the −10° to −5°C range. The amount of snowfall on 13 and 16 September was extreme, being considerably greater than the 99th percentile of July to October 1979–2017 climatology (fig. S2).

The exceptional amount of snowfall over the Eastern Weddell Sea during the AR events that occurred before the opening of the polynya (i.e., 11 to 13 September 2017), likely enhanced the melting via insulation effects (43). The thermal conductivity of the snow being an order of magnitude lower than that of sea ice (44), a deep snowpack over thin ice in the winter can effectively decouple the sea ice from the atmosphere and insulate it from frigid polar air, which prevents its growth (43, 45). In addition, the sea ice surrounding the freshly opened polynya continued to be affected by the subsequent synoptic-scale ARs and associated snowfall and radiative forcing. These ARs affected a larger area than that of the polynya (Fig. 4 and fig. S3). This may have prevented sea ice growth around the polynya and contributed to maintaining it open even after the decay of the ARs/cyclones.

The AR-induced alteration of the energy balance seen in the time series, averaged over the polynya area, was also observed over the whole area affected by the ARs (i.e., Fig. 4). For instance, the exceptional AR event during 11 to 13 September 2017, which immediately preceded the opening of the polynya, significantly altered the radiative fluxes at the surface and at the top of atmosphere

(TOA). During this period, all-sky upwelling LW radiation maps show that less LW radiation by 100 W m^{-2} was able to leave the TOA in the AR area compared to surrounding areas (Fig. 4A), with a minimum cooling efficiency around 0°E that corresponded to the area of maximum PWAT and total column cloud liquid water content (Fig. 2, D and H). This reservoir of energy was retained in the atmosphere and radiated back to the surface. The maps of all-sky downwelling LW radiation at the surface (Fig. 4B) show that the sea ice surface below the AR footprint received 250 W m^{-2} more energy than surrounding areas in the same sector.

The areas of elevated surface LW fluxes on 13 September 2017 (Fig. 4B) highlight a similar spatiotemporal coincidence with the large precipitable water amount and cloud liquid water content (Fig. 2, D and H) brought by the ARs (Fig. 2, B and E), i.e., both were colocated within the area in which the polynya subsequently opened (Fig. 1D).

The signature of ARs is clearly apparent in the LW radiation anomalies (Fig. 4C) where the LW radiation retained in the atmosphere and within the AR was higher than the climatological mean by fully 3 SDs. The increase in LW radiation at the surface resulted in a positive total energy flux (Fig. 4D). For instance, and on 12 September 2017 at 1300 UTC, the area affected by the AR received more than +25 W m^{-2} instantaneous energy flux (Fig. 4C). The increase in input of energy at the surface by LW radiation contributed to the increase of surface skin temperature, which was anomalously positive by more than 10°C within the AR footprint (Fig. 4, E and F).

The sea ice concentration in the polynya area decreased during the 11 to 13 September 2017 event from 85% to below 50% by the end of the day on 13 September 2017 (Fig. 4E). It is worth noting that this reduction in sea ice concentration occurred before the arrival of the cyclone above the polynya area (Fig. 4F). This implies that the sea ice cover was primarily reduced by the AR-induced warming during the 4 days preceding the opening and then was followed by additional decrease via sea ice drift by strong cyclonic winds i.e., divergence in the ice motion field (37). Without the reduction in the sea ice cover by the ARs, the cyclones may have not been able to open alone the compact winter sea ice cover in this region.

The radiative forcing induced by ARs increased the vulnerability of the polynya-region sea ice to dynamical forcing by the cyclones that developed behind the ARs in the subsequent hours. ARs are also known to favor more intense cyclones by providing additional latent heat (9), which may have increased the impact of ARs on the sea ice both thermodynamically (by sea ice melt) and dynamically (by strengthening the cyclones).

All AR events were followed by the development of synoptic-scale deep cyclones situated to the west of the ARs [Figs. 2 (B, D, and F) and 4F and fig. S1A]. These cyclones were studied in detail in (37) and were found to cause wind-stress forcing on the ice cover, already weakened by the ARs, to trigger a polynya event. In this sense, ARs and cyclones seem to work as a coupled system wherein intense ARs weaken the sea ice cover and strengthen the cyclones by providing more water vapor for latent heat release (9). Moreover, the cyclones enhance the poleward transport of moisture and heat, which, in turn, deteriorates the sea ice cover (as demonstrated here). Therefore, we conclude that the Weddell Polynya event in 2017 resulted from ice melt and inhibited nighttime refreezing initiated by the ARs and immediately followed by wind-driven ice divergence caused by the cyclones.

The ERA5-derived surface wind speeds during these events in the order of 30 m s^{-1} persisted for the entire duration of the combined AR/cyclone events (37). From the histogram analysis (Fig. 5), the surface winds associated with the AR/cyclone on 13 and 16 September 2017 were exceptional, with the daily mean 10-m wind speed being greater than the 99th percentile relative to August to September climatology (Fig. 5F).

The observed temperature increase at the surface, and ice loss during the AR events preceding the polynya opening, were also evident during the events after the opening i.e., on 16, 17, and 28 September 2017. This, in turn, resulted in a significant enlargement of the already opened polynya (figs. S1 to S3).

The exceptional nature of the ARs in 2017

Histograms of several daily-averaged ERA5 variables (Fig. 5) provide a climatological context for the AR events in 2017 that provoked the Weddell Polynya event. The distribution of daily mean IVT for all August to September 1979–2017 days reveals that the persistent AR event on 12 and 13 September was among the most intense on record with the daily mean IVT values above the 95th percentile of all August to September climatology (Fig. 5A) and the hourly IVT values peaking well above the 99th percentile (Fig. 3). The net LW radiation at the surface generated by this event was above the 95th percentile

of the full-year climatology for 1979–2017 (fig. S2D), which led to a positive daily mean net radiation at the surface, and the associated values were greater than the 95th percentile of all August to September 1979–2017 days (Fig. 5B). The extreme AR events resulted in exceptional warmth at the surface with daily mean skin temperature and 2-m air temperature above the 95th percentile of all August to September climatological values (Fig. 5, C and D).

The distribution of daily mean snow accumulation during the AR events on 13 and 16 September was exceptionally unusual compared to the record, being well above the 99th percentile (Fig. 5E). More particularly, snow accumulation during the AR on 16 September, 2 days after the initial opening of the polynya, was unique relative to the record (Fig. 5E), which may have prevented the bottom growth of new sea ice because of insulation effects at the sea ice in the surroundings of the newly opened polynya (43).

The synoptic-scale cyclones that immediately followed the AR events were associated with exceptionally high 10-m wind speeds compared to the August to September climatology (Fig. 5F). The daily mean 10-m wind speeds during the cyclones on 13 and 16 September were greater than the 99th percentile, whereas those associated with the cyclone on 1 September were above the 95th percentile (Fig. 5F). The exceptional nature of the AR/cyclone events in 2017 highlights the crucial role of the heat and moisture transported by the ARs in
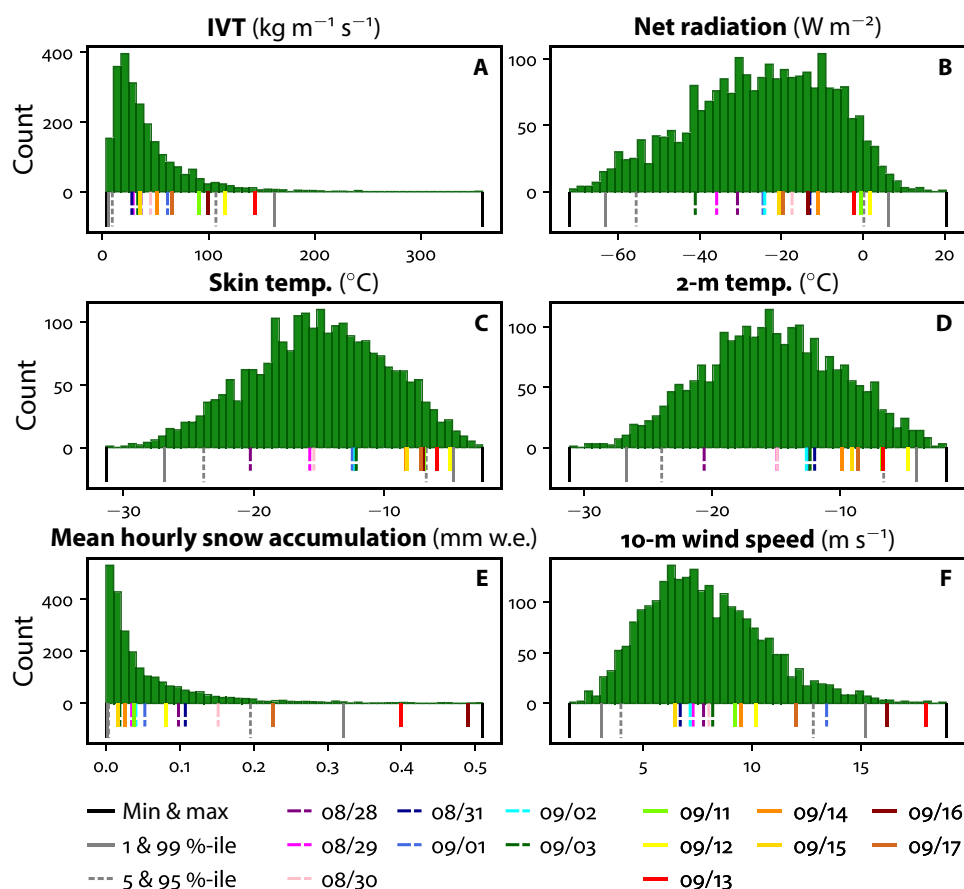

Fig. 5. The exceptional nature of the 2017 AR events. Histograms showing the distribution of daily mean values for all August to September climatology during 1979–2017, spatially averaged over 2°W to 8E°E and 63°S to 67°S of the following: (**A**) IVT, (**B**) net radiation at the surface, (**C**) skin temperature, (**D**) 2-m surface air temperature, (**E**) mean hourly snow accumulation in millimeter water equivalent, and (**F**) 10-m wind speed. The colored vertical lines correspond to daily mean values during the 28 August–17 September 2017 period. The gray lines correspond to the 1st and 99th percentiles, the black lines correspond to the minimum and maximum values, and the dashed gray lines correspond to the 5th and 95th percentiles.

initiating a polynya event and the role of the exceptionally strong winds carried by the cyclones in accentuating a decrease in sea ice concentration via sea ice drift.

ARs and polynya occurrence in November 1973

Although the Weddell Polynya was spotted in satellite observations for the first time in winter 1974 (46), this was in fact 1 year after its actual initial opening in November 1973 (identified here by inspecting the satellite data). Because the polynya opened in the late-spring season, it did not refreeze during that sea ice year, and in fact, it remained open for three consecutive winters probably because of the altered ocean circulation (28). It was not until September 2017 that the second large opening occurred (as discussed in the previous section), after a short-lived and smaller Weddell Polynya event in August 2016 that was also associated with an intense AR and severe storm activity (38). The first opening in 1973 occurred at 63°S and 5°E to 12°E, which is 2° to the north and 3° to the east of the initial opening in 2017. This position was coincident with the most southern extremity of the AR on 20 November 1973, which was further north compared to the ARs in 2017 (Fig. 6A), as was the polynya opening. The simultaneous nature of the openings and the AR footprints in each polynya event implies that ARs, by virtue of their effect on LW radiation, were a key contributing factor to this phenomenon, and one that has been overlooked to date.

The AR maps shown in Fig. 6 reveal a band of high IVT emanating on 18 November 1973 from the tropics (25°S, i.e., a lower latitude than in 2017) and propagating poleward over the South Atlantic toward Antarctica with its core axis around 0°E (Fig. 6A). The PWAT associated with the AR was anomalously high, with positive values exceeding 2.5 SDs from the climatological mean (Fig. 6B). Total column of cloud liquid water in the AR sector was higher than 100 g m^{-2} (Fig. 6C). Highly positive anomalies of LW radiation, of fully 3 SDs above the climatological mean, were seen in the AR sector (Fig. 6D). This demonstrated a high retention of LW radiation in the atmosphere within the AR, coincident with the high content of water vapor (Fig. 6B) and cloud liquid water (Fig. 6C).

The AR and an associated large deep cyclone to the west and centered at 20°W (Fig. 6A) approached the Weddell Sea on 18 November 1973 at 0000 UTC and remained until 20 November at 0600 UTC. During this 2-day period, the sea ice concentration decreased significantly (Fig. 6E) and the polynya opened first on 22 November 1973 at 63°S (Fig. 6F).

Given these factors, we propose that the loss of sea ice in the polynya area at the time of polynya opening was associated with the downwelling LW flux anomalies. ARs, elevated water vapor and cloud liquid water content, increased LW fluxes, and decreased sea ice concentration are concomitant and common features of each of the polynya opening events examined, i.e., 1973, 2016 (not shown), and 2017.

SUMMARY AND CONCLUSIONS

This study reveals the occurrence of intense ARs in the late-winter season in the Weddell Sea and demonstrates their role in initiating major opening events of the Weddell Polynya. By virtue of their effect in significantly increasing downwelling LW fluxes (because of strongly increased high water vapor amount and cloud liquid water content), warm air temperatures and precipitation in the form of

heavy warm snow, ARs are identified as an important factor in these phenomena—and one which has been overlooked to date.

Combining satellite observations and reanalysis data, we identified the occurrence of intense ARs that preceded the two major Weddell Polynya opening events in November 1973 and September 2017 by 1 to 2 days. By investigating the effects of ARs on sea ice conditions during these two events, we found that the resulting warm air advection and increase in LW fluxes at the surface, due to the presence of opaque clouds and increased water vapor content in the atmosphere within the AR area, significantly reduced the sea ice thickness and concentration.

The exceptional atmospheric conditions during the AR events under scrutiny increased the sea ice vulnerability to the wind-driven ice divergence associated with the cyclones that formed shortly behind the ARs [see (37)]. The role of the synoptic-scale ARs was crucial in initiating and maintaining the polynya by melting ice and preventing refreezing. Cyclones, a ubiquitous feature around Antarctica, may have not been able to trigger a polynya event without the presence of the ARs, which preconditioned the ice cover over a large area. The role of the ARs was in twofold, persistently fragilizing the ice cover through radiative effects (before and after the opening of the polynya) and likely strengthening the cyclones by providing additional water vapor for latent heat release (9, 10).

Here, we propose that while the special atmospheric conditions induced by the ARs and the accompanying cyclones play the role of triggers in the two major Weddell Polynya events in 1973 and 2017, ocean processes are essential to the polynya longer-term preconditioning, enlargement, and maintenance (32, 36, 38). As reported in (38), warm near-surface ocean temperatures of unknown origin were observed in oceanic float data during the polynya formation in September 2017 [see also (34)]. The study also concluded that while the formation of Weddell Polynya events may be explained by upward salt transfer from convective mixing, what controls the initial openings is still unknown. On the basis of our analysis, ARs and associated warm conditions are likely at the origin of this warming and, together with the subsequent cyclones, control the initial openings.

Francis et al. (37) have shown that winter of 2017 were exceptional in terms of heat and moisture transport from midlatitudes toward Antarctica. In this study, we have presented evidence that the most significant transport occurred in the form of ARs, supported by atmospheric blocking ahead of the ARs associated with a pronounced zonal wave number three pattern during this particular winter (i.e., 33 and 37).

The new results presented here highlight the need for focused research into the potentially important wider effects of ARs on the Antarctic sea ice environment and ecosystem (as well as other polynyas). This relates (among other things) to (i) their modulation of LW and SW radiation fluxes, surface temperature, and snowfall; (ii) their possible contribution to observed patterns of change/variability in Antarctic sea ice coverage (47); and (iii) their possible role in recent Antarctic ice-shelf disintegration events, e.g., Larsen B in 2002 (48).

Developing improved understanding of ARs, their effect on the coupled sea ice–ocean-atmosphere–ice sheet biological system and the possible regional and seasonal dependencies involved, is of increasing importance. Under projected future climate change, the frequency of AR events is predicted to increase by ~50% globally and 60% in the southern midlatitudes (49), as well as a general poleward shift in AR landfall location (5). It is also anticipated that ARs will become longer and wider and will entail stronger and more effective
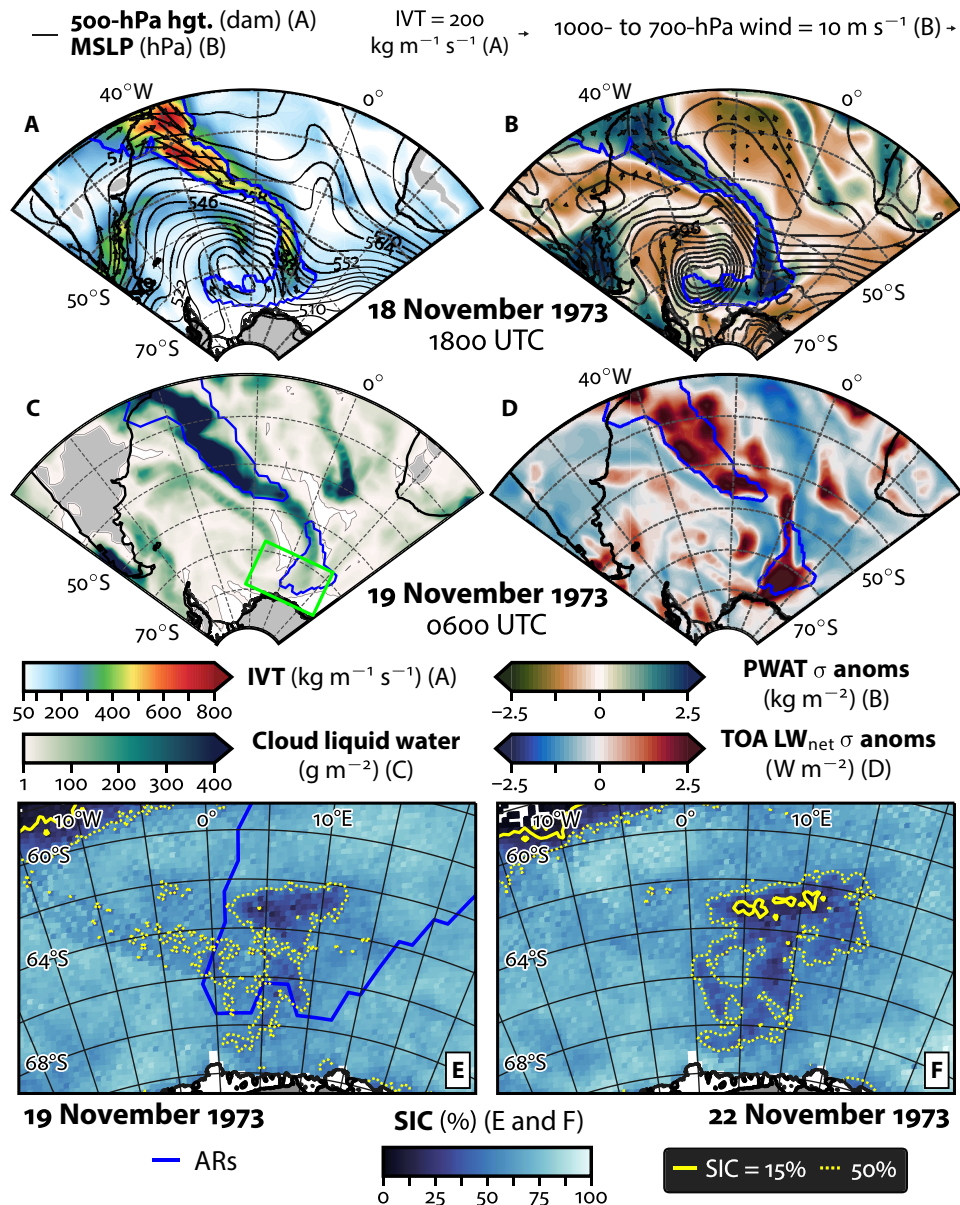
Fig. 6. The 1973 polynya event. JRA55 reanalysis maps on 18 November 1973 at 1800 UTC of the following: (**A**) IVT magnitude (shaded) and direction (black vectors) and geopotential heights at 500 hPa in black contours. Red contours represent areas with climatological IVT PR above the 85th percentile. (**B**) Standardized anomalies of precipitable water (shaded), 1000- to 700-hPa mean winds in vectors, and MSLP in black contours. (**C**) Total column cloud liquid water (shaded) on 19 November 1973 at 0600 UTC. (**D**) Standardized anomalies of TOA LW (shaded) on 19 November 1973 at 0600 UTC relative to the 1970–2000 climatological reference period. Positive anomalies of TOA LW flux represent less outgoing LW radiation. (**E**) Daily sea ice concentration in the small domain represented in the green box in (D) from Nimbus 5 on 19 November 1973. (**F**) Same as (E) but on 22 November 1973. The solid yellow line is the 15% contour, and the dotted yellow line is the 50% contour. The 15% contour of sea ice concentration was used to delineate the polynya. (A to E) The ARs are outlined in blue contours.

mechanisms for the atmospheric transport of high levels of integrated water vapor between the low-/mid-southern latitudes and the Antarctic Ocean and continent. Because of the increased atmospheric moisture in a warmer climate, the intensity of AR-related precipitation is predicted to increase as well (5).

As stated in Introduction, research into the regional role of ARs in the coupled Antarctic sea ice–ocean-atmosphere–ice sheet system lags behind that in the Arctic. There, recent studies (3, 22) have confirmed that AR events can cause sea ice melt or inhibit sea ice growth due to the increased cloud cover–downward LW radiation mechanism, especially during winter when there is no shortwave radiation to offset the positive LW cloud radiative forcing. No similar long-term study of the impacts of moisture transport events on the entire Antarctic sea ice cover has been conducted to determine whether a similar mechanism is at work there, which constitutes a further avenue for future research. This would also improve the prediction of likely sea ice change and variability under future climate change.

Last, the possibility that winter AR events in the Antarctic may also affect the seasonal evolution of the sea ice environment through the subsequent summer months (and beyond) deserves consideration. In the Arctic, it has been observed that ARs not only affect the surface temperature over the sea ice but also induce warming waves that propagate downward through the sea ice interior to affect its properties and also reduce ice basal growth (8). This process has been shown to influence the Arctic sea ice thickness at the onset of seasonal melt in spring, and the probability of similar processes in the relatively thin Antarctic sea ice pack merits investigation. An additional major unknown relates to the possible effects of ARs in increasing regional snowfall/accumulation over the Antarctic sea ice zone—to potentially affect regional sea ice melt/persistence given its insulative properties and its contribution to snow-ice formation (15). We hope that this study will motivate such investigations.

MATERIALS AND METHODS

The atmospheric analysis is based on data from the Japanese 55-year Reanalysis (JRA55) (50) for the 1973 period and from the ERA5 reanalysis (51) for the 2017 period. The ERA5 radiative fluxes are provided as mean rates over the hour before the given time step (e.g., the output at 1200 UTC is the mean rate during 1100 to 1200 UTC), whereas the JRA55 fluxes are three hourly averages (e.g., the output at 1200 UTC is the mean rate during 0900 to 1200 UTC). Because of the strong diurnal signal in LW radiation over land, we used the values for the specific time of day to calculate anomalies relative to the 1970–2000 distribution for JRA55 and 2008–2017 for ERA5. For example, for LW anomalies mapped at 1200 UTC on 13 September 2017, the distribution of all September 1200 UTC values during the climatological reference period was used to calculate anomalies.

Furthermore, to investigate the anomalous character of the atmospheric conditions during the 2017 Polynya event, we calculated for several atmospheric variables, hourly standardized anomalies, and percentile ranks relative to all hourly ERA5 August to September values during the full record (1979–2017). In addition, a climatological histogram analysis has been performed for the 2017 Polynya event where daily averaged variables during September 2017 are compared to the climatology with August to September 1979–2017 as climatological reference period. The histograms represent the distribution of daily mean values spatially averaged over −2°W to 8°E and − 63°S to −67°S, for all August to September months during 1979–2017.

ARs are detected and identified through analysis of IVT at six-hourly time steps from JRA55 and ERA5 reanalysis data, using a modified version of the detection algorithm used in (3). The IVT values within the 1000- to 200-hPa layer are first calculated over the Southern Hemisphere poleward of 10°S, according to the formula

$$\mathrm{IVT} \ = \ \frac{1}{g} \int\limits_{1000\,\mathrm{hPa}}^{200\,\mathrm{hPa}} q\boldsymbol{V}\, dp \tag{1}$$

where $g = 9.80665$ m s^{-2} is gravitational acceleration, q and $\boldsymbol{V}$ are specific humidity (kg kg^{-1}) and vector wind (m s^{-1}) at the given pressure level, respectively, and dp is the difference between adjacent pressure levels. Pressure levels are incremented by 50 hPa between 1000 and 500 hPa and by 100 hPa between 500 and 200 hPa, while IVT units are kg m^{-1} s^{-1}. The climatological percentile rank of IVT (IVT PR) at each time step is then calculated by comparing the IVT value at each grid cell to the distribution of all IVT values at that grid cell for the given month during the climatological reference period for each reanalysis. The climatological reference periods used here are 1970–2000 for JRA55 and 2008–2017 for ERA5.

Following (3), the AR detection procedure begins by finding contiguous regions wherein actual or "raw" IVT values are above a certain threshold and the IVT PR value is ≥85%. The minimum IVT threshold is set to 50 kg m^{-1} s^{-1} [as opposed to 150 kg m^{-1} s^{-1} in (3)] because IVT values near Antarctica are generally less than in the Northern Hemisphere high latitudes (40). Potential ARs are then filtered by applying size, location, length, length-to-width ratio, and mean transport direction criteria. These requirements ensure that the identified features are long, narrow, coherent bands of poleward moisture transport in (and connecting) the middle and polar latitudes of the Southern Hemisphere, i.e., they bear the characteristics of ARs. See (3) for additional details on the AR detection and mapping algorithm.

Sea ice extent and concentration data were taken from the Nimbus 5 satellite observations (52) for the 1973 period, whereas for the 2017 period, they were obtained from the National Oceanic and Atmospheric Administration/National Snow and Ice Data Center (NSIDC) Climate Data Record of Passive Microwave Sea Ice Concentration, version 3 and its near-real-time version (53). These data are mapped on the NSIDC polar stereographic grid with a nominal 25 km by 25 km grid cell area at both daily and monthly temporal resolution. Sea ice thickness was derived from the satellite Soil Moisture and Ocean Salinity mission (54).

For surface and TOA radiative flux quantities during the 2017 event, we use the satellite-derived CERES Synoptic (CERES-SYN) version 3 dataset (55). CERES-SYN provides daily LW surface and TOA flux quantities over a 1° × 1° resolution grid in both clear-sky and all-sky conditions and covering March 2000 to present.

SUPPLEMENTARY MATERIALS

REFERENCES AND NOTES

1. F. M. Ralph, M. Dettinger, D. Lavers, I. V. Gorodetskaya, A. Martin, M. Viale, A. B. White, N. Oakley, J. Rutz, J. R. Spackman, H. Wernli, J. Cordeira, Atmospheric rivers emerge as a global science and applications focus. *Bull. Am. Meteorol. Soc.* **98**, 1969–1973 (2017).

2. D. Nash, D. Waliser, B. Guan, H. Ye, F. M. Ralph, The role of atmospheric rivers in extratropical and polar hydroclimate. *J. Geophys. Res. Atmos.* **123**, 6804–6821 (2018).

3. K. S. Mattingly, T. L. Mote, X. Fettweis, Atmospheric river impacts on Greenland Ice Sheet surface mass balance. *J. Geophys. Res. Atmos.* **123**, 8538–8560 (2018).

4. J. D. Wille, V. Favier, A. Dufour, I. V. Gorodetskaya, J. Turner, C. Agosta, F. Codron, West Antarctic surface melt triggered by atmospheric rivers. *Nat. Geosci.* **12**, 911–916 (2019).

5. A. E. Payne, M-E. Demory, L. R. Leung, A. M. Ramos, C. A. Shields, J. J. Rutz, N. Siler, G. Villarini, A. Hall, F. M. Ralph, Responses and impacts of atmospheric rivers to climate change. *Nat. Rev. Earth Environ.* **1**, 143–157 (2020).

6. H. Binder, M. Boettcher, C. M. Grams, H. Joos, S. Pfahl, H. Wernli, Exceptional air mass transport and dynamical drivers of an extreme wintertime Arctic warm event. *Geophys. Res. Lett.* **44**, 12028–12036 (2017).

7. S. H. Doyle, A. Hubbard, R. S. W. van de Wal, J. E. Box, D. van As, K. Scharrer, T. W. Meierbachtol, P. C. J. P. Smeets, J. T. Harper, E. Johansson, R. H. Mottram, A. B. Mikkelsen, F. Wilhelms, H. Patton, P. Christoffersen, B. Hubbard, Amplified melt and flow of the Greenland ice sheet driven by late-summer cyclonic rainfall. *Nat. Geosci.* **8**, 647–653 (2015).

8. P. O. G. Persson, M. D. Shupe, D. Perovich, A. Solomon, Linking atmospheric synoptic transport, cloud phase, surface energy fluxes, and sea-ice growth: Observations of midwinter SHEBA conditions. *Climate Dynam.* **49**, 1341–1364 (2017).

9. Z. Zhang, F. M. Ralph, M. Zheng, The relationship between extratropical cyclone strength and atmospheric river intensity and position. *Geophys. Res. Lett.* **46**, 1814–1823 (2019).

10. I. Simmonds, K. Keay, J. A. Tristram Bye, Identification and climatology of southern hemisphere mobile fronts in a modern reanalysis. *J. Climate* **25**, 1945–1962 (2012).

11. A. Alberello, L. Bennetts, P. Heil, C. Eayrs, M. Vichi, K. MacHutchon, M. Onorato, A. Toffoli, Drift of pancake ice floes in the winter Antarctic Marginal Ice Zone during polar cyclones. *J. Geophys. Res. Oceans* **125**, e2019JC015418 (2020).

12. V. A. Squire, Ocean wave interactions with sea ice: A reappraisal. *Annu. Rev. Fluid Mech.* **52**, 37–60 (2020).

13. A. Sorteberg, J. E. Walsh, Seasonal cyclone variability at 70°N and its impact on moisture transport into the Arctic. *Tellus A* **60**, 570–586 (2008).

14. J. Grieger, G. C. Leckebusch, C. C. Raible, I. Rudeva, I. Simmonds, Subantarctic cyclones identified by 14 tracking methods, and their role for moisture transports into the continent. *Tellus A* **70**, 1–18 (2018).

15. R. A. Massom, S. E. Stammerjohn, R. C. Smith, M. J. Pook, R. A. Iannuzzi, N. Adams, D. G. Martinson, M. Vernet, W. R. Fraser, L. B. Quetin, R. M. Ross, Y. Massom, H. R. Krouse, Extreme anomalous atmospheric circulation in the West Antarctic Peninsula region in austral spring and summer 2001/02, and its profound impact on sea ice and Biota. *J. Climate* **19**, 3544–3571 (2006).

16. L. N. Boisvert, A. A. Petty, J. C. Stroeve, The impact of the extreme winter 2015/16 Arctic cyclone on the Barents–Kara Seas. *Mon. Weather Rev.* **144**, 4279–4287 (2016).

17. W. Neff, Atmospheric rivers melt Greenland. *Nat. Clim. Change* **8**, 857–858 (2018).

18. M. Oltmanns, F. Straneo, M. Tedesco, Increased Greenland melt triggered by large-scale, year-round cyclonic moisture intrusions. *Cryosphere* **13**, 815–825 (2019).

19. K. S. Mattingly, T. L. Mote, X. Fettweis, D. van As, K. van Tricht, S. Lhermitte, C. Pettersen, R. S. Fausto, Strong summer atmospheric rivers trigger Greenland Ice Sheet melt through spatially varying surface energy balance and cloud regimes. *J. Climate* **33**, 6809–6832 (2020).

20. I. V. Gorodetskaya, M. Tsukernik, K. Claes, M. F. Ralph, W. D. Neff, N. P. M. van Lipzig, The role of atmospheric rivers in anomalous snow accumulation in East Antarctica. *Geophys. Res. Lett.* **41**, 6199–6206 (2014).

21. H.-S. Park, S. Lee, Y. Kosaka, S. W. Son, S. W. Kim, The impact of Arctic winter infrared radiation on early summer sea ice. *J. Climate* **28**, 6281–6296 (2015).

22. S. Lee, T. Gong, S. B. Feldstein, J. A. Screen, I. Simmonds, Revisiting the cause of the 1989–2009 Arctic surface warming using the surface energy budget: Downward infrared radiation dominates the surface fluxes. *Geophys. Res. Lett.* **44**, 10654–10661 (2017).

23. K. Stramler, A. D. Del Genio, W. B. Rossow, Synoptically driven Arctic winter states. *J. Climate* **24**, 1747–1762 (2011).

24. C. Woods, R. Caballero, The role of moist intrusions in winter Arctic warming and sea ice decline. *J. Climate* **29**, 4473–4485 (2016).

25. B. M. Hegyi, P. C. Taylor, The unprecedented 2016–2017 Arctic sea ice growth season: The crucial role of atmospheric rivers and longwave fluxes. *Geophys. Res. Lett.* **45**, 5204–5212 (2018).

26. B. Luo, L. Wu, D. Luo, A. Dai, I. Simmonds, The winter midlatitude-Arctic interaction: Effects of North Atlantic SST and high-latitude blocking on Arctic sea ice and Eurasian cooling. *Climate Dynam.* **52**, 2981–3004 (2019).

27. A. P. Worby, C. A. Geiger, M. J. Paget, M. L. Van Woert, S. F. Ackley, T. L. DeLiberty, Thickness distribution of Antarctic sea ice. *J. Geophys. Res.* **113**, C05S92 (2008).

28. A. L. Gordon, J. C. Comiso, Polynyas in the Southern Ocean. *Sci. Am.* **258**, 6 (1988).

29. D. G. Barber, R. A. Massom, The role of sea ice in Arctic and Antarctic polynyas. *Elsevier Oceanogr. Ser.* **74**, 1–54 (2007).

30. C. O. Dufour, A. K. Morrison, S. M. Griffies, I. Frenger, H. Zanowski, M. Winton, Preconditioning of the Weddell Sea polynya by the ocean mesoscale and dense water overflows. *J. Climate* **30**, 7719–7737 (2017).

31. J. Blunden, D. S. Arndt, State of the Climate in 2016. *Bull. Am. Meteorol. Soc.* **98**, Si–S280 (2017).

32. B. Jena, M. Ravichandran, J. Turner, Recent reoccurrence of large open-ocean polynya on the Maud Rise seamount. *Geophys. Res. Lett.* **46**, 4320–4329 (2019).

33. E. Schlosser, F. A. Haumann, M. N. Raphael, Atmospheric influences on the anomalous 2016 Antarctic sea ice decay. *Cryosphere* **12**, 1103–1119 (2018).

34. S. Swart, E. C. Campbell, C. H. Heuze, K. Johnson, J. L. Lieser, R. Massom, M. Mazloff, M. Meredith, P. Reid, J.-B. Sallee, S. Stammerjohn, Return of the Maud Rise polynya: Climate litmus or sea ice anomaly? [in State of the Climate in 2017]. *Bull. Am. Meteorol. Soc.* **99**, S188–S189 (2018).

35. H. Zanowski, R. Hallberg, J. L. Sarmiento, Abyssal ocean warming and salinification after Weddell polynyas in the GFDL CM2G coupled climate model. *J. Phys. Oceanogr.* **45**, 2755–2772 (2015).

36. W. G. Cheon, A. L. Gordon, Open-ocean polynyas and deep convection in the Southern Ocean. *Sci. Rep.* **9**, 6935 (2019).

37. D. Francis, C. Eayrs, J. Cuesta, D. Holland, Polar cyclones at the origin of the reoccurrence of the Maud Rise polynya in Austral winter 2017. *J. Geophys. Res.* **124**, 5251–5267 (2019).

38. E. C. Campbell, E. A. Wilson, G. W. K. Moore, S. C. Riser, C. E. Brayton, M. R. Mazloff, L. D. Talley, Antarctic offshore polynyas linked to Southern Hemisphere climate anomalies. *Nature* **570**, 319–325 (2019).

39. I. Rudeva, I. Simmonds, Variability and trends of global atmospheric frontal activity and links with large-scale modes of variability. *J. Climate* **28**, 3311–3330 (2015).

40. I. V. Gorodetskaya, T. Silva, H. Schmithüsen, N. Hirasawa, Atmospheric river signatures in radiosonde profiles and reanalyses at the Dronning Maud Land coast, East Antarctica. *Adv. Atmos. Sci.* **37**, 455–476 (2020).

41. S. Nihashi, K. Ohshima, Relationship between ice decay and solar heating through open water in the Antarctic sea ice zone. *J. Geophys. Res.* **106**, 16767–16782 (2001).

42. C. Eayrs, D. Holland, D. Francis, T. Wagner, R. Kumar, X. Li, Understanding the seasonal cycle of Antarctic sea ice extent in the context of longer-term variability. *Rev. Geophys.* **57**, 1037–1064 (2019).

43. R. M. Graham, P. Itkin, A. Meyer, A. Sundfjord, G. Spreen, L. H. Smedsrud, G. E. Liston, B. Cheng, L. Cohen, D. Divine, I. Fer, A. Fransson, S. Gerland, J. Haapala, S. R. Hudson, A. M. Johansson, J. King, I. Merkouriadi, A. K. Peterson, C. Provost, A. Randelhoff, A. Rinke, A. Rösel, A. Sennéchael, V. P. Walden, P. Duarte, P. Assmy, H. Steen, M. A. Granskog, Winter storms accelerate the demise of sea ice in the Atlantic sector of the Arctic Ocean. *Sci. Rep.* **9**, 9222 (2019).

44. G. A. Maykut, Energy exchange over young sea ice in the central Arctic. *J. Geophys. Res.* **83**, 3646–3658 (1978).

45. I. Merkouriadi, B. Cheng, R. M. Graham, A. Rösel, M. A. Granskog, Critical role of snow on sea ice growth in the Atlantic Sector of the Arctic Ocean. *Geophys. Res. Lett.* **44**, 10479–10485 (2017).

46. F. D. Carsey, Microwave observation of the Weddell Polynya. *Mon. Weather Rev.* **108**, 2032–2044 (1980).

47. C. L. Parkinson, A 40-y record reveals gradual Antarctic sea ice increases followed by decreases at rates far exceeding the rates seen in the Arctic. *Proc. Natl. Acad. Sci. U.S.A.* **116**, 14414–14423 (2019).

48. R. A. Massom, T. A. Scambos, L. G. Bennetts, P. Reid, V. A. Squire, S. E. Stammerjohn, Antarctic ice shelf disintegration triggered by sea ice loss and ocean swell. *Nature* **558**, 383–389 (2018).

49. V. Espinoza, D. E. Waliser, B. Guan, D. A. Lavers, F. M. Ralph, 2018: Global analysis of climate change projection effects on atmospheric rivers. *Geophys. Res. Lett.* **45**, 4299–4308 (2018).

50. S. Kobayashi, Y. Ota, Y. Harada, A. Ebita, M. Moriya, H. Onoda, K. Onogi, H. Kamahori, C. Kobayashi, H. Endo, K. Miyaoka, K. Takahashi, The JRA-55 Reanalysis: General specifications and basic characteristics. *J. Meteorol. Soc. Japan* **93**, 5–48 (2015).

51. H. Hersbach, B. Bell, P. Berrisford, S. Hirahara, A. Horányi, J. Muñoz-Sabater, J. Nicolas, C. Peubey, R. Radu, D. Schepers, A. Simmons, C. Soci, S. Abdalla, X. Abellan, G. Balsamo, P. Bechtold, G. Biavati, J. Bidlot, M. Bonavita, G. Chiara, P. Dahlgren, D. Dee, M. Diamantakis, R. Dragani, J. Flemming, R. Forbes, M. Fuentes, A. Geer, L. Haimberger, S. Healy, R. J. Hogan, E. Hólm, M. Janisková, S. Keeley, P. Laloyaux, P. Lopez, C. Lupu, G. Radnoti, P. Rosnay, I. Rozum, F. Vamborg, S. Villaume, J. N. Thépaut, The ERA5 global reanalysis. *Q. J. Roy. Meteorol. Soc.* **146**, 1999–2049 (2020).

52. H. J. Zwally, J. Comiso, C. Parkinson, W. Campbell, F. Carsey, P. Gloersen, Antarctic Sea Ice. Satellite Passive-Microwave Observations. NASA SP-4591973-1976 (1983).

53. W. Meier, F. Fetterer, M. Savoie, S. Mallory, R. Duerr, J. Stroeve, NOAA/NSIDC Climate Data Record of Passive Microwave Sea Ice Concentration, Version 3. [Antarctic, daily, monthly], (NSIDC: National Snow and Ice Data Center, Boulder, Colorado USA, 2017); https://doi.org/10.7265/N59P2ZTG [accessed 20 June 2019].

54. L. Kaleschke, X. Tian-Kunze, N. Maaß, A. Beitsch, A. Wernecke, M. Miernecki, G. Müller, B. D. Fock, A. M. U. Gierisch, K. Heinke Schlünzen, T. Pohlmann, M. Dobrynin, S. Hendricks, J. Asseng, R. Gerdes, P. Jochmann, N. Reimer, J. Holfort, C. Melsheimer, G. Heygster, G. Spreen, S. Gerland, J. King, N. Skou, S. S. Søbjærg, C. Haas, F. Richter, T. Casal, SMOS sea ice product: Operational application and validation in the Barents Sea marginal ice zone. *Remote Sens. Environ.* **180**, 264–273 (2016).

55. B. A. Wielicki, B. R. Barkstrom, E. F. Harrison, R. B. Lee III, G. L. Smith, J. E. Cooper, Clouds and the Earth's Radiant Energy System (CERES): An Earth observing system experiment. *Bull. Am. Meteorol. Soc.* **77**, 853–868 (1996).

Science Advances

On the crucial role of atmospheric rivers in the two major Weddell Polynya events in 1973 and 2017 in Antarctica
Diana Francis, Kyle S. Mattingly, Marouane Temimi, Rob Massom and Petra Heil

ARTICLE TOOLS	http://advances.sciencemag.org/content/6/46/eabc2695
SUPPLEMENTARY MATERIALS	http://advances.sciencemag.org/content/suppl/2020/11/09/6.46.eabc2695.DC1
REFERENCES	This article cites 53 articles, 1 of which you can access for free http://advances.sciencemag.org/content/6/46/eabc2695#BIBL
PERMISSIONS	http://www.sciencemag.org/help/reprints-and-permissions

Use of this article is subject to the Terms of Service